J Appl Electrochem (2009) 39:2093–2105
DOI 10.1007/s10800-009-9895-1

ORIGINAL PAPER

Physico-chemical characterization of IrO_2–SnO_2 sol-gel nanopowders for electrochemical applications

Silvia Ardizzone · Claudia L. Bianchi · Laura Borgese · Giuseppe Cappelletti · Cristina Locatelli · Alessandro Minguzzi · Sandra Rondinini · Alberto Vertova · Pier Carlo Ricci · Carla Cannas · Anna Musinu

Received: 28 September 2008 / Accepted: 12 March 2009 / Published online: 6 May 2009

Abstract Mixed tin–iridium oxide ($Sn_{0.85}Ir_{0.15}O_2$) nanoparticles at low Ir content (15 mol%) were prepared by the sol–gel preparative route, varying calcination temperatures in the range 450–550 °C. The crystal structures, the phase composition and crystallite sizes were analyzed by X-ray powder diffraction (XRD). The local order of the materials was investigated by Raman spectroscopy. X-ray photoelectron spectroscopy (XPS) analysis revealed the variation of the Ir surface state with the temperature of firing. The morphology of crystallites and the aggregates were analyzed by high resolution transmission electron microscopy (HRTEM) and scanning electron microscopy (SEM), respectively. Nitrogen physisorption by BET method was adopted to evaluate the particle surface area and the mesopore volume distribution. Electrochemical properties of the Ti-supported powders were evaluated by cyclic voltammetry (CV) and quasi steady-state voltammetry.

S. Ardizzone · C. L. Bianchi · G. Cappelletti · C. Locatelli · A. Minguzzi (✉) · S. Rondinini · A. Vertova
Dipartimento di Chimica Fisica ed Elettrochimica, Università degli Studi di Milano, Via Golgi 19, 20133 Milan, Italy
e-mail: alessandro.minguzzi@unimi.it

L. Borgese
Department of Mechanical and Industrial Engineering, The University of Brescia, Via Branze 38, 25123 Brescia, Italy

P. C. Ricci
Department of Physics, University of Cagliari, S.P. Monserrato-Sestu Km 0.700, 09042 Monserrato, CA, Italy

C. Cannas · A. Musinu
Department of Chemical Sciences, University of Cagliari, S.P. Monserrato-Sestu Km 0.700, 09042 Monserrato, CA, Italy

Keywords Nanocomposites · Electrocatalysis · Sol–gel · Tin oxide · Iridium oxide · Dimensionally stable anodes

1 Introduction

The electrochemical applications of IrO_2-based materials range from sensors [1, 2] to electrochromic devices [3, 4] to electrocatalytic coatings of dimensionally stable anodes (DSAs) in chlor-alkali technology [5, 6]. More recently acid water electrolysis, finalized to the production of high purity hydrogen, has become a key process in the conversion and storage of energy from renewable sources. Moreover, thanks to the development of the technology of solid polymer electrolyte cells, reversible proton exchange membranes electrolysers/fuel cells devices are becoming increasingly attractive for environmentally respectful distributed systems.

In PEM electrolysers, electrode coatings are generally pre-prepared particles, applied as an "ink" to the membrane to ensure both good contact between the electrocatalytic layer and the solid membrane electrolyte, and a viable route for the reactant access and the gaseous products removal [7, 8].

The choice of electrode coating is mainly restricted to IrO_2 or RuO_2-based materials, which conjugate high electrocatalytic activity for oxygen evolution reaction (OER) with high stability in acidic environment.

Although RuO_2 has a higher electrocatalytic activity than IrO_2 and lower costs, its service life is about 20 times shorter [9] thus shifting the interest toward IrO_2-based mixed oxides in which the precious metal is diluted by a cheap hosting matrix. Additives of non noble elements (e.g. Ta, Ti, Zr, Ce, Sb, Nb, Sn) are used to reduce the cost of

the catalyst and/or to improve the coating properties [10, 11]. Numerous binary and ternary oxide mixtures have been presented in the literature as anode materials for O_2 evolution in acidic media [12–19] but still the amount of precious Ir is rather high. For example, optimal IrO_2 contents are for IrO_2–ZrO_2 80 mol%, for IrO_2–Ta_2O_5 55–70 mol% and for IrO_2–TiO_2 40 mol% below which electrode service lives decrease sharply [15]. Binary SnO_2–IrO_2 mixtures [7, 8, 16–20] result especially stable under extensive O_2 evolution; consequently electrodes containing more than 10% of precious metal oxide are known to proceed in acidic solutions with kinetic parameters close to those of pure IrO_2 [16–18]. In our recent work on ternary Sn–Ir–Ta systems [14], synthesized by a controlled sol–gel route at low (500 °C) calcination temperature, we confirmed the interesting behaviour of the Sn–Ir composites at 15 mol% of Ir, even in the absence of the improving effect of Ta.

Moreover, IrO_2-based oxides have been recently investigated as energy storage materials [21] and as electrocatalysts for oxygen reduction reaction (ORR) [22–24], hydrogen evolution reaction (HER) [25–27] and electrooxidation of organic pollutants [28, 29].

On these grounds, we have recently extended our investigations to the bulk and surface features of nanocrystalline IrO_2–SnO_2 systems, prepared by sol–gel procedure, adopting tin alkoxide and $IrCl_3$ as starting materials, while varying the calcination temperature in the 450–550 °C range.

The adopted synthetic route contributes significantly to the tailoring of the material and consequently to its final performance, the more so in the case of multicomponent nanocrystalline systems. Recently we documented the effectiveness of the low-temperature sol–gel synthetic process to produce tailored nanostructured materials also in the case of the base matrix of SnO_2 [30, 31].

In the present work particular attention is dedicated to the analysis of the structural features of the SnO_2–IrO_2 mixed oxides due to the importance played by the formation of a solid solution between the components in enhancing the material stability [13]. CV and quasi steady-state voltammetric curves under OER conditions provide the electrochemical features of the mixed oxide, grown on Ti nets, unbiased by the contribution/cooperation of additives, implicit in gas diffusion electrodes (GDE) and membrane electrode assemblies (MEA). The consistency between the electrochemical response of the plain powder and the Ti-grown material was also confirmed by means of the cavity-microelectrode [32, 33].

The electrochemical behaviour is then related to bulk and surface properties as determined by an extended physicochemical characterization (X-Ray Powder Diffraction—XRPD, Raman spectroscopy, Transmission Electron Microscopy—TEM/HRTEM). Results obtained by refinement of XRD patterns are analysed also with respect to parallel results obtained by Raman spectroscopy and by TEM and HRTEM. By XPS analyses the surface state and composition are investigated to evidence possible surface segregation-enrichment of the components.

2 Experimental

All the chemicals were of reagent grade purity and were used without further purification; doubly distilled water passed through a Milli-Q apparatus (MilliQ® Millipore System) was used to prepare solutions and suspensions.

2.1 Sample preparation

The Ir doped SnO_2 particles were obtained by room-temperature sol–gel reaction, as previously reported in the case of pure SnO_2 (water/alkoxide molar ratio of 81.7 and a water/propanol molar ratio of 8.5) [30, 31], starting from $Sn(C_4H_9O)_4$ and adopting $IrCl_3 \cdot 3H_2O$ such as to obtain a final $IrO_2/(IrO_2 + SnO_2)$ 20% weight (Sn/Ir molar ratio = 5.9). The dried xerogels were thermally treated at 450, 500 and 550 °C for 2 h under oxygen flux, after 3 h temperature ramp. The calcined powders are labelled as Sn_T or SnIr_T, where T denotes the firing temperature.

The Ti-supported powder electrodes are prepared by dipping-and-drying 1 cm × 1 cm × 0.05 cm Ti rhomboidal meshes (R4, previously sandblasted and pickled in aqueous 10wt% Oxalic acid at 80 °C for 1 h) in the same conditions adopted for the particles.

The procedure consists in dipping each electrode support in the reactor used for powder synthesis, for 1 min, then drying it under a warm air flow for 2 min and finally completing the drying process at 80 °C for 9 min. Each cycle is repeated 10 times. Ti supported xerogels are then subjected to the same treatment followed by the unsupported powders. The weight of the deposit after calcination is about a few milligrams. The layers grown on titanium are labelled Ti-SnIr_T, where T is the calcination temperature.

2.2 Sample characterisation

Room temperature X-ray powder diffraction (XRPD) patterns were collected between 10 and 80° (2θ range $\Delta 2\theta = 0.02°$, time per step = 10 s, scan speed = 0.002°/s) with a Siemens D500 diffractometer, using Cu Kα radiation. Rietveld refinement has been performed using the GSAS software suite [34] and its graphical interface EXPGUI [35]. The broadening due to the instrumental contributions was taken into account by means of a calibration performed with a standard Si powder. Components

of peak broadening due to strain were not varied in the fitting procedure. The convergence was in any case satisfactory.

The backgrounds have been subtracted using a shifted Chebyshev polynomial. The diffraction peak's profile has been fitted with a pseudo-Voigt profile function. Site occupancies and the overall isotropic thermal factors have been varied. The average diameter of the crystallites, d, was estimated from the most intense reflection of the SnO_2 cassiterite phase using the Scherrer equation.

"Calculated" surface areas have been obtained by elaborating the crystallite sizes obtained from X-ray diffraction spectra by means of the following formula [36]:

$$S_{\text{calc.}} = \frac{6 \times 10^4}{d \times \rho}$$

where ρ = tin oxide density (7.0 g cm^{-3}); d = crystallite diameter (Å).

The relation assumes that the particles are composed by single crystals, have a spherical geometry and that both porosity and surface roughness are absent. Consequently this relation provides only approximate estimates of the surface area to be compared with the experimental one.

Specific surface areas were determined by the classical BET procedure using a Coulter SA 3100 apparatus.

Micro Raman spectra (RS) have been collected in air at room temperature with a Raman spectrometer (Dilor XY800) operating with the 514.5 nm line of an argon ion laser (Coherent Innova 90C-4) in back scattering geometry. The signal, dispersed with a 1200 grooves/mm grating, was detected by a 1024 × 256 liquid Nitrogen cooled charge coupled detector (CCD), with a spectral resolution of $\leq$0.7 cm^{-1}.

X-ray photoelectron spectra were taken in an M-probe apparatus (Surface Science Instruments). The source was monochromatic AlK radiation (1486.6 eV). The binding energies (BE) were corrected for specimen charging by referencing the C 1 s peak to 284.6 eV, and the background was subtracted using Shirley's method [37]. The deconvolutions were performed using only Gaussian line shapes. The peaks were fitted without BE or FWHM (Full Width at Half Maximum) constraints. The accuracy of the reported BE can be estimated to be ±0.1 eV. With a monochromatic source, an electron flood gun is required to compensate the build up of positive charge on the samples during the analyses, when insulating samples are analysed: a value of 5 eV has been selected.

The particle morphology was examined by scanning electron microscopy using a LEO 1430.

TEM dark field (DF) images and selected-area electron diffraction (SAED) patterns were obtained on a JEOL 200 CX microscope equipped with a tungsten cathode operating at 200 kV. The powders were dispersed in n-octane by sonication and a drop of the dispersion deposited on a carbon film supported by a copper grid. Particle size was obtained by measuring the average diameter of the particles from different parts of the grid for an average number of particles close to 500 for each sample. Particle size distribution is represented with histograms and average particle size calculated with a log normal distribution [38].

HRTEM images were obtained with a JEM 2010 UHR equipped with a Gatan Imaging Filter (GIF) and a 794 slow scan CCD camera. Energy Filtered (EF) images were obtained with an aperture of a 25 eV slit.

The electrochemical properties of Ti-supported powders were investigated by cyclic voltammetry, CV, and quasi steady-state voltammetry. Voltammetries were performed using AMEL System 5000 (AMEL Instruments) potentiostat/galvanostat driven by CorrWare (Scribner Associates Inc., Souther Pines, U.S.A.) in a 3-electrode cell, equipped with a Pt counter-electrode. Scanning rates were 2, 5, 10, 20, 50, 100, 200, 500 and 1000 mV s^{-1}. Cycling was extended until full reproducibility between two consecutive cycles was obtained. Before CV recording, solutions were degassed by N_2 bubbling.

Quasi steady-state polarization curves were recorded stepwise at 10 mV/min in the 1.4–2.0 V potential range. At the end of the last backward scan the electrodes were kept at 0.9 V for 5 min.

CV measurements were also performed by means of the cavity-microelectrode (C-ME), a micro-recessed electrode which allows the support of small quantities (1–10 ng) of the calcined powders. The C-ME was prepared as described by [39, 40]. The cavity was filled with material particles using the electrode as a pestle. The filling of the cavity was controlled with the optical microscope, and at the same time, it was verified that no particle remained on the head outside the cavity.

All measurements were performed in $HClO_4$ 0.1 M. The solutions were prepared with highly deionized water (MilliQ® Millipore System). All potentials were referred to the reversible hydrogen electrode (RHE).

3 Results

In the following, results will be presented discussing both the electrochemical behaviour and the structural, morphological and spectroscopic features of SnO_2 and $Sn_{0.85}Ir_{0.15}O_2$ nanoparticles as a function of calcination temperatures (450, 500, 550 °C).

3.1 Structural and morphological features

XRD analysis was performed on annealed materials. The whole-pattern Rietveld refinement suggests the presence of

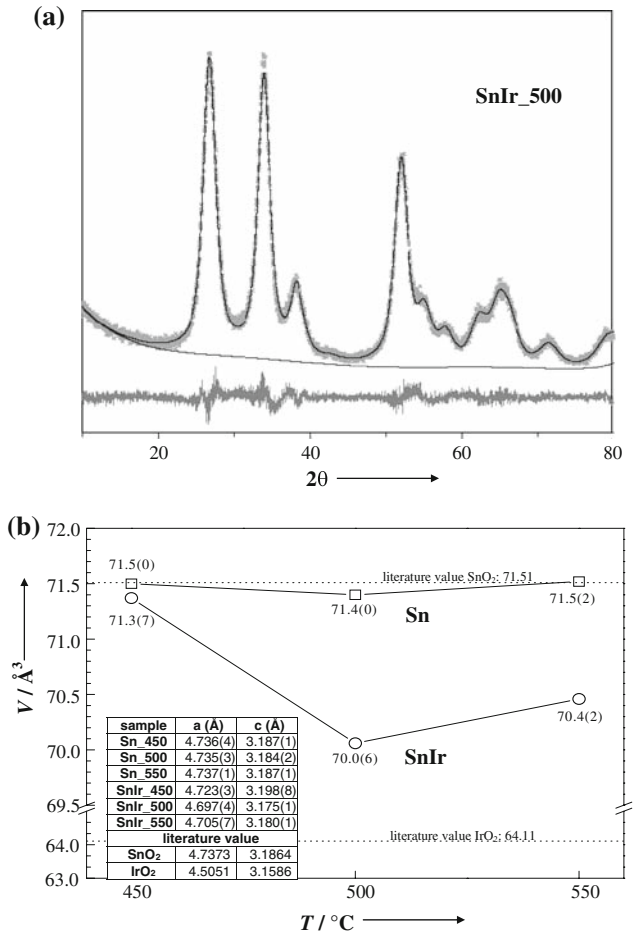

Fig. 1 (**a**) X-Ray diffraction line of SnIr_500 sample and relative Rietveld refinement; (**b**) Cassiterite cell volume as a function of the firing temperature. Squares, pure SnO_2; circles, $Sn_{0.85}Ir_{0.15}O_2$. *Inset*: cell parameters

only the SnO_2 cassiterite structure, for both pure and doped samples (Fig. 1a). No crystalline phase related to separate IrO_2 phases can be detected with the exception of the Ir-doped powder calcined at the highest temperature, 550 °C, in which the amount of a separate IrO_2 phase can be estimated to be around 4%.

Figure 1b shows the variation of the unit cell volume of the cassiterite structure for undoped and $Sn_{0.85}Ir_{0.15}O_2$ samples with the heating temperature. The figure reports also, for the sake of comparison, the literature unit cell volume of both SnO_2 and IrO_2 (dashed lines). The cell volume of the undoped samples is quite invariable with the calcination temperature; on the contrary the addition of iridium provokes a general decrease in cell volumes the more so in the case of the 500 °C heated sample. The unit cell parameters (a, c), shown in the inset of the Fig. 1b confirm the same behaviour. The contraction of the cassiterite unit cell volume upon addition of iridium can be interpreted as the result of the substitution, in the lattice, of a bigger ion, Sn^{4+} (0.083 nm) by a smaller ion, Ir^{4+} (0.077 nm). The comparison between the size of the two ionic radii and of the relative Pauling electronegativities is seen to fulfil the Hume-Rothery rule for solid solutions [41] and allows to suggest that a solid solution between iridium and tin oxides is formed in the present case. Literature data concerning the possible formation of solid solutions in Ir–Sn oxide powders are rather controversial. Murakami et al. [42] report, for Ir–SnO_2 composites prepared via a sol–gel method, XRD patterns consistent with a solid solution between iridium and tin oxide with the lattice parameters showing a linear relationship over the entire composition range. Similar evidences are reported by Marshall et al. [19] in the case of $Ir_xSn_{1-x}O_2$ powders prepared by a wet method and afterwards calcined at 500 °C; in the case of samples obtained by a thermal decomposition procedure and subsequently fired at identical temperature, the same authors observe the production of two separate phases, highly dispersed into one another. Liu et al. [43] observed, for IrO_2–SnO_2 electrodes prepared by sol–gel from $SnCl_4$, that the oxide coating was the mixture of independent phases IrO_2 and SnO_2. Other authors [8, 44] have found either no or very limited solubility of IrO_2 in SnO_2 at high temperatures. In the present work, a highly intermixed Ir–Sn material is probably formed during the initial sol–gel step thus allowing a stable or metastable solid solution to be formed during the final annealing step.

The cell parameters are affected by the temperature adopted for the calcination. The two samples heated at the lower T (450, 500 °C) do not show any appreciable presence of segregate IrO_2. However the contraction of the cell volume of the two samples is markedly different. On the grounds of a literature correlation between cell volume and iridium doping for the cassiterite structure, the cell parameters of the 500 °C sample could suggest a total reticular substitution of all the Ir added in the synthesis. This instead does not occur in the case of the 450 °C sample, which shows almost no variation with respect to the pure SnO_2 structure. In the case of this sample the incomplete hydrolysis/combustion of the starting Ir salt could be suggested. The possible residual presence of the salt in the final product cannot be ruled out only on the basis of XRD results, since the salt displayed a non-characteristic, X-ray amorphous pattern. The sample heated at 550 °C shows a marked contraction with respect to pure SnO_2, but to a lower extent with respect to the 500 °C, possibly also due to the partial segregation of IrO_2.

A further information on the structural features of the Ir–Sn composites can be obtained by the trend of the crystallite sizes, obtained by both evaluation of the X-ray peaks by the Scherrer's equation and elaboration of TEM analyses (Fig. 2a). The mean crystal sizes of undoped and Ir-doped powders increase with the calcination temperature;

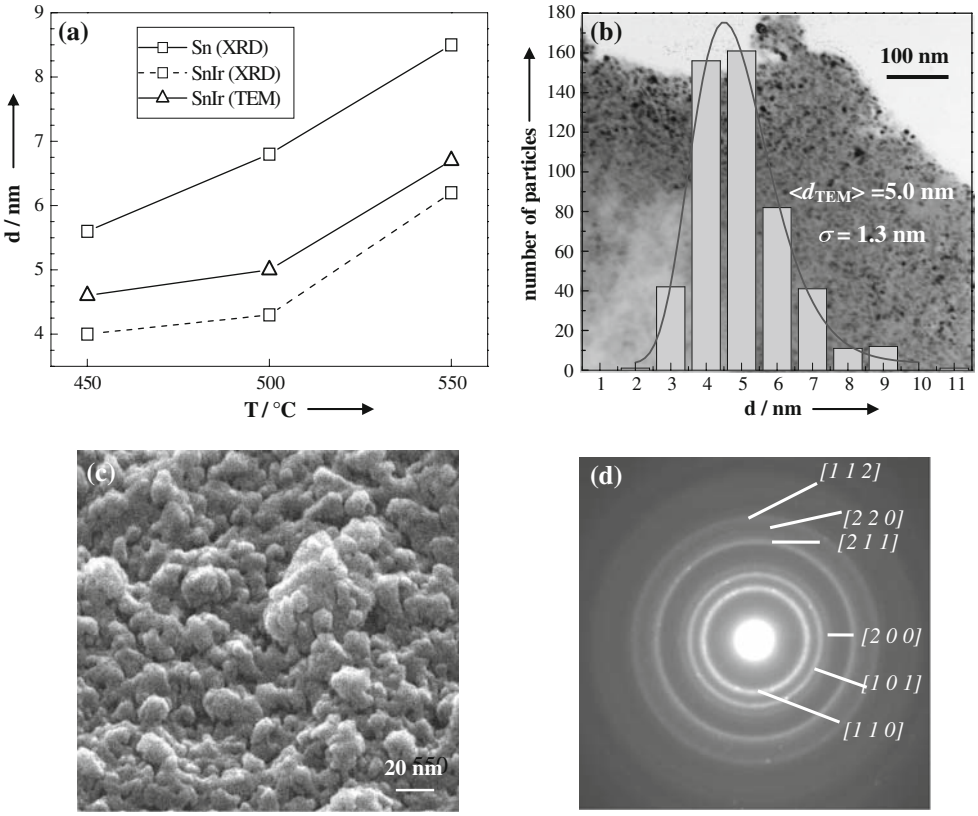

Fig. 2 (**a**) Crystallite sizes as a function of the firing temperature; SnIr_500 sample: (**b**) Dark field TEM image and crystallite size distribution; (**c**) SEM image; (**d**) SAED pattern of the cassiterite phase

Table 1 Experimental ($S_{B.E.T.}$), calculated ($S_{calc.}$) surface areas and relative per cent of sintering for SnO_2 and $Sn_{0.85}Ir_{0.15}O_2$ samples calcined at different temperatures

sample	$S_{B.E.T.}$ ($m^2\ g^{-1}$)	$S_{calc.}$ ($m^2\ g^{-1}$)	% sintering
Sn_450	64.5	153	58
Sn_500	52.5	126	58
Sn_550	41.0	100	59
SnIr_450	79.6	214	63
SnIr_500	56.7	199	71
SnIr_550	37.5	138	73

in particular the samples with Ir show lower particle diameters, as reported in the literature [19], confirming the lower crystallinity of the Ir-doped samples. The TEM dark field (DF) images of these samples show rounded nanocrystals with average diameter that gradually increases from 4.6 to 6.7 nm by increasing the treatment temperature from 450 to 550 °C. The particle size distribution for the three samples is quite narrow, considering that the standard deviation is about 30% in all the cases. A slight broadening can be observed going from the sample treated at 450 °C to the one at 550 °C; the standard deviation increases from 28 to 34% accordingly. Figure 2b shows the case of the sample calcined at 500 °C.

Table 1 reports the experimental surface area ($S_{B.E.T.}$) and the one calculated from X-ray data ($S_{calc.}$, see the experimental part). The values of the surface area of undoped and Ir-doped materials with increasing the calcination temperature closely mirror the trend of the crystallite sizes (the smaller the crystallite sizes, the larger the surface areas). The comparison between the $S_{B.E.T.}$ and the $S_{calc.}$ from X-ray diffraction data and the evaluation of the consequent degree of sintering (Table 1) shows that the actual particles can be considered to be mainly composed by aggregated crystallites, especially for the Ir-doped samples (as shown in the SEM micrograph of the sample calcined at 500 °C Fig. 2c).

The selected-area electron diffraction (SAED) patterns confirm the presence of cassiterite phase in all the samples; Fig. 2d reports the representative case of the SnIr_500 sample. The EF HRTEM images confirm the spherical morphology of the nanocrystals (Fig. 3), already suggested on the grounds of TEM (DF) images. A set of fringes can be observed in Fig. 3, which correspond to the lattice (101) planes of the cassiterite phase.

3.2 Spectroscopic characterizations

In the case of nanometer materials disorder and nanoparticle size strongly influence the vibrational properties of the system. When the nanoparticle size is decreased, the bands associated with the classical modes of the material shift and broaden according to the phonon dispersion curves; further,

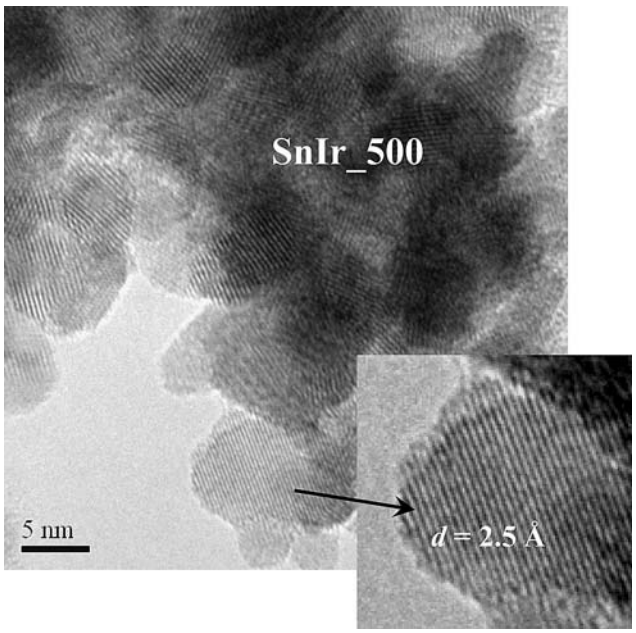

Fig. 3 HRTEM micrograph of the SnIr_500 sample; *inset*: fringes corresponding to the (101) lattice plane of the cassiterite structure

with a decrease in grain size, bands other than the classical ones can be manifested by addition to the normal Raman modes of the single crystal [45]. In the case of nanometer SnO_2 the Raman spectrum peaks have been attributed, in the literature, to different contributions: one group of peaks is the same as that for single-crystals and is attributed to the crystalline phase; the second group, which is observed only in the case of nanometer particles with small grain size, is attributed to surface modes [46, 47].

On the grounds of these reported data the Raman spectra of the present pure SnO_2 samples calcined at the three temperatures (Fig. 4a), were deconvoluted, according to Dieguez et al. [47], by using three Lorentzian curves, representing the classical modes, and three Gaussians representing the surface modes. The expected Raman active modes for both the crystalline phase and the surface are observed (see Table 2) in agreement with literature results.

The same procedure can be applied to the mixed samples, where again the Raman spectrum has been fitted by using three Gaussians (surface modes) and three Lorentzian modes for the crystalline phase (Fig. 4b). The doped samples show a larger surface Raman efficiency which can be related to a larger disorder of the nanoparticle surface shell or, in a more general way, to a larger disorder of the structure.

The results of the fitting procedures, reported in Table 2, can be commented. The E_g band at 476–477 cm^{-1} shows little dependence on either the particle size (i.e. the calcination temperature) or the Ir doping due to its low intensity. The A_{1g} band, which is well appreciable, is the most responsive to both the Ir doping and the size of the crystals. The literature values reported for pure crystalline SnO_2 range around 638–634 cm^{-1}, but the frequency may shift to lower values with the decrease of the particle size. Actually Sn_550, which presents the largest crystallite sizes (see the previous sections), shows a slightly larger value with respect to the other undoped samples. The A_{1g} band occurs at 752 cm^{-1} in the case of pure IrO_2. The shift to larger frequencies of this band, in the case of the doped samples, could support the formation of a solid solution between SnO_2 and IrO_2. From results in the Table 2, sample SnIr_500 could be considered the sample with the largest degree of substitution while SnIr_450 the one with the lowest one. The positions of the third "crystalline" band, B_{2g}, for SnO_2 and IrO_2, are 782 and 728 cm^{-1} respectively. In this case the effects of the size of the crystal and of the doping shift the band in the same direction. The spectral positions of the bands reported in Table 2 appear to be very congruent with the structural data presented in the previous sections. Evaluation of X-ray patterns of all mixed samples showed, in fact, the presence of a IrO_2–SnO_2 solid solution as apparent from the shift of the A_{1g} modes of the composites; further, volume cell data showed that the maximum distortion of the lattice occurred in the case of the SnIr_500 sample, in agreement with the larger shift observed for the A_{1g} band in Table 2 in the case of this sample. The overlapping of IrO_2 modes with the surface mode S_3 and the B_{1g} mode of the SnO_2 crystal cannot either support or exclude the presence of the small amount of a separate IrO_2 phase observed by X-ray in the case of SnIr_550.

In order to analyze the relation between the change in the Raman spectrum and the temperature of the sample treatment, the ratios between the areas of the surface Raman modes and of the crystalline ones have been reported, for both the pure and the mixed samples, as a function of the crystallite sizes, obtained by X-ray diffraction (Fig. 5). The figure shows that for each series the surface contribution decreases with the temperature, the more so in the case of the mixed samples; further, for each temperature, the weight of the surface appears to be much larger in the case of the mixed samples than for the pure SnO_2. The decrease of the surface contribution with the increase in crystal size is the direct result of the decrease in the number of surface atoms while the number of core atoms increases simultaneously. Thus, the scattering intensity from the surface phonons will decrease while the scattering intensity from the internal phonons will increase gradually. The much larger weight of the surface modes with respect to the crystalline ones shown by the doped samples is very interesting and, to the author's best knowledge, has not been reported previously in the literature, in the case of mixed samples. The effect is the result

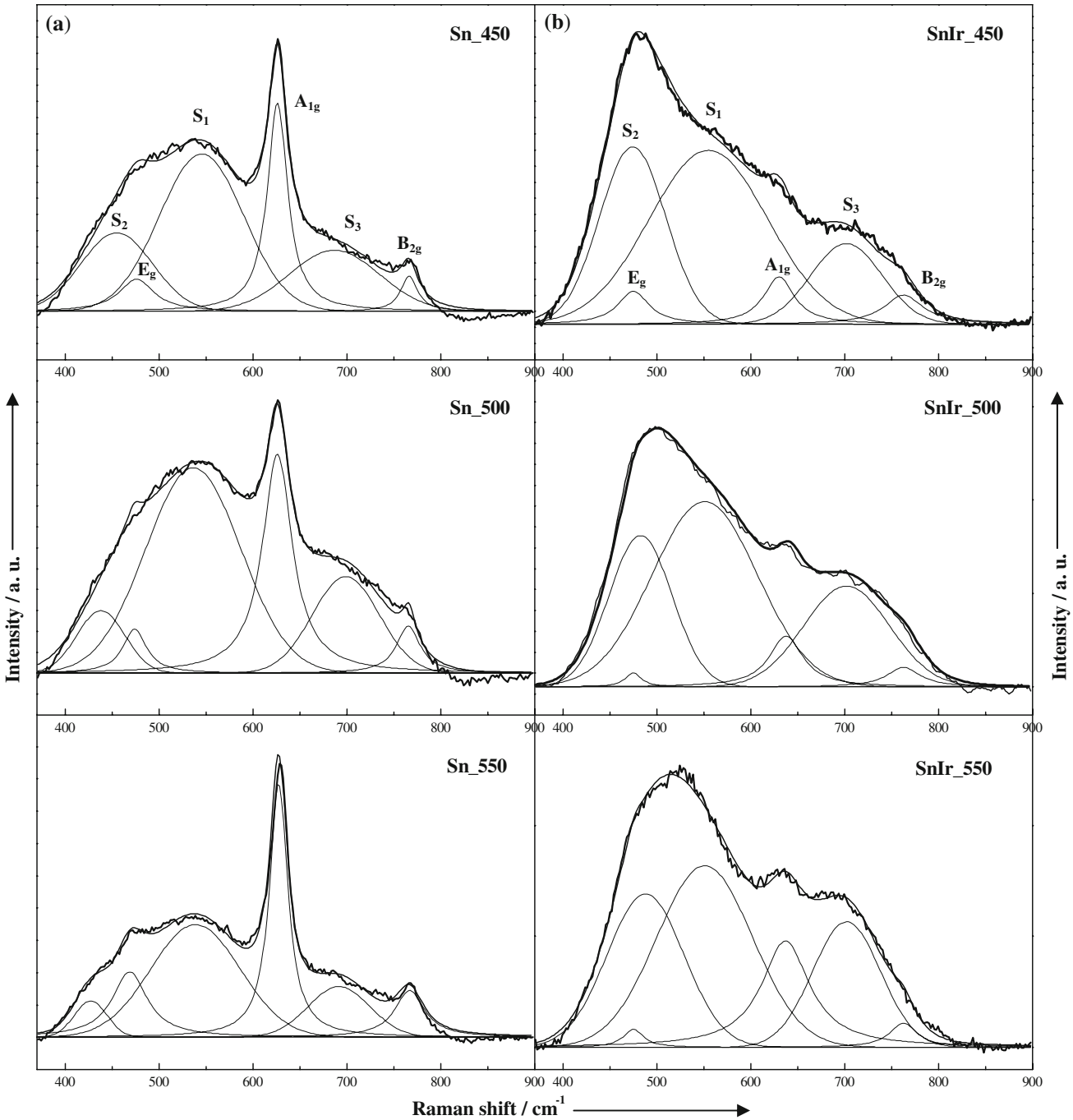

Fig. 4 Raman spectra of: (**a**) pure SnO_2 and (**b**) $Sn_{0.85}Ir_{0.15}O_2$ fired at the three temperatures

of the small size of the crystallites combined with the disorder produced by the doping, in the external layers of the particles.

Survey XPS spectra were recorded for all samples. No significant presence of impurities was observed, except for the ubiquitous carbon contaminant. In the case of the latter element, only the C 1 s peak at 284.6 eV (due to –CH– species) was present.

The chemical state of tin, iridium and oxygen in the composite particles was examined. Both the Sn and Ir investigated regions (3d and 4f, respectively) do not give rise to a single photoemission peak, but to a closely spaced doublet due to the j–j spin-orbit coupling.

The Sn 3d region shows, in any case, the regular doublet with peaks at 486.7 and 495.2 eV in agreement with literature data for tin oxides [48] and with previous results

Table 2 Raman shift of the most important bands observed in the SnO_2 and $Sn_{0.85}Ir_{0.15}O_2$ samples at different calcination temperatures. Modes A_{1g}, B_{2g} and E_g correspond to the classical vibration modes while bands S_1, S_2 and S_3 correspond to surface modes

	Wavenumber(cm^{-1})					
Band	Sn_450	Sn_500	Sn_550	SnIr_450	SnIr_500	SnIr_550
E_g	476	475	476	477	476	477
A_{1g}	626	626	629	633	638	637
B_{2g}	765	766	767	758	763	763
S_1	545	545	539	569	551	551
S_2	455	454	427	476	483	488
S_3	686	696	691	702	702	702

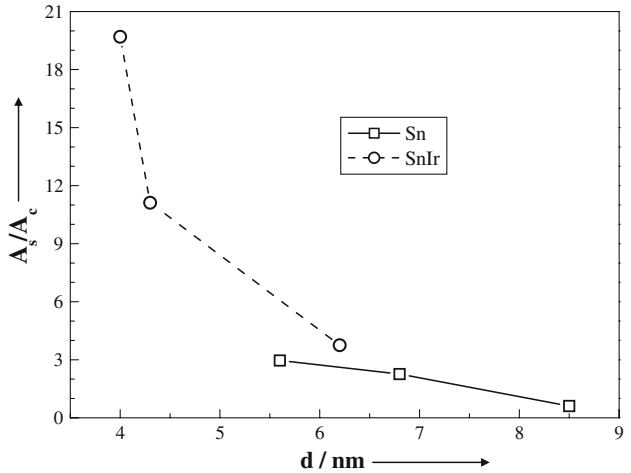

Fig. 5 Ratio of the summed area of bands S_1 and S_2 with respect to the area of the band for the A_{1g} mode as a function of the crystallite size obtained by XRD for the pure tin oxide and the Ir doped materials

obtained by us on pure tin oxide [31]. No significant differences could be appreciated in the binding energies (BE) of tin as an effect of either the presence of Ir or of the calcination temperature. This result is in agreement with literature data, on SnO_2–IrO_2 oxides, reported by Atanasoska et al. [49] and Marshall et al. [19].

The Sn/Ir atomic ratios (Table 3, 2nd column) are, in any case, comparable with the bulk values (5.95), and show a slight Ir surface enrichment for calcination temperatures of 500 °C or higher.

The Ir 4f region is very complex and shows the presence of more than one species. There is considerable disagreement in the literature about the nature of the components of the Ir 4f peak in the case of IrO_2, either pure or in mixture. Several authors [50, 51] attribute the main component to Ir(III) (61.6–62.0 eV), and the second component at higher B.E. (62.3–62.8 eV) to Ir(IV). Other authors, instead, attribute the same doublets respectively to Ir(IV) and to Ir in a higher oxidation state [2, 52]. In the present case the Ir 4f peaks were initially, tentatively, fitted by two components.

Table 3 Atomic ratios and different Ir $4f_{7/2}$ peak components (with relative position, eV and intensity, %) obtained by XPS determinations for $Sn_{0.85}Ir_{0.15}O_2$ samples calcined at different temperatures

Sample	Sn/Ir	Cl/Ir	Ir	eV	%
SnIr_450	6.5	1.7	III	61.9	50.0
			IV	62.5	16.6
			>IV	63.6	33.4
SnIr_500	6.0	1.3	III	61.6	38.4
			IV	62.5	39.3
			>IV	63.5	22.3
SnIr_550	6.1	1.1	III	61.7	28.4
			IV	62.5	35.5
			>IV	63.5	36.1

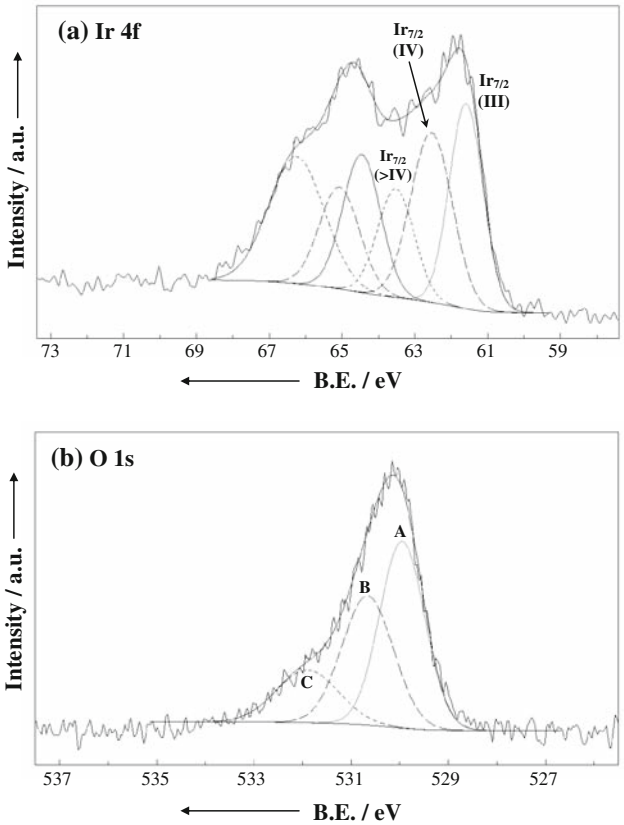

Fig. 6 XPS spectra of SnIr_500 sample: (**a**) Ir $4f_{7/2,5/2}$ doublets relative to the different Ir spectral components; (**b**) Oxygen 1 s peak

This procedure however was not successful since χ square values were not satisfying and, moreover, the peaks, fitting the $4f_{5/2}$ component, showed far too high FWHM values (>4 eV). Consequently the present Ir 4f peaks were fitted assuming the presence of three components, by using only Gaussian line shapes and without BE or FWHM constraints. The best fit of all the peaks yielded three components which were attributed respectively to Ir(III) at 61.7, to Ir(IV) at 62.6 and to Ir in an oxidation state higher than four at 63.6 eV

(Fig. 6a), in agreement with results obtained by us previously in the case of ternary Sn–Ta–Ir oxide mixtures [14].

Also the oxygen 1 s peak of the mixed oxides is complex and shows the presence of several components. In the case of pure iridium oxide the oxygen peak is generally fitted by three components, corresponding to three different oxygen species, i.e. lattice oxide, hydroxide, surface OH groups or undissociated water [2, 52, 53]. In the present case the situation is more complicated due to the presence of Sn oxides or oxohydroxides. Figure 6b reports the O 1 s peak of a doped sample calcined at 500 °C. The best fit yields three components, which can be attributed respectively to lattice oxygen in SnO_2 (529.9 eV, A component), hydroxide in $Sn(OH)_4$ or lattice oxygen in IrO_2 (530.7 eV, B component), OH groups in $Ir(OH)_4$ or $IrO(OH)_2$ plus possible surface OH species (531.9 eV, C component). The role played by the temperature of calcination on the Ir 4f peak components is represented by the surface atomic ratios in Table 3 (4th, 5th, 6th column). The Ir(III) peak component is shown to decrease progressively from a maximum value of around 50% at 450 °C to a value lower than 30% at 550 °C; the Ir(IV) component shows a marked increase in passing from 450 to 500 °C and then levels off to a slightly lower value at 550 °C. The Ir(>IV) component shows the smallest temperature dependence and presents the maximum value at 550 °C.

3.3 Electrochemical behaviour

The electrochemical characterization is performed in two separate potential windows, namely 0.4–1.4 V vs RHE and 1.4–2.0 V vs RHE, which provide complementary information.

The 0.4–1.4 V window is widely used because it highlights key material features, like the charge storage capacity and the proton diffusivity of the layer, while excluding the H_2 and O_2 evolution reactions.

In fact, it includes the pseudo-capacitive proton intercalation process:

$$MO_x(OH)_y + \delta H^+(\text{solution}) + \delta e^-(\text{oxide}) \rightarrow MO_{x-\delta}(OH)_{y+\delta} \quad (1)$$

which is at the base of the good performance of the material as supercapacitor, sensor or electrocatalyst. As repeatedly observed by several authors [30, 31, 54, 55], the voltammetric quantity of charge accumulated in the chosen potential interval can be used as a measure of the active area of the electrocatalyst. More specifically, the number of most accessible active sites normalized to the total number of sites, given by the ratio $Q_{out}/Q_{tot} = \lim[(Q)\ v \rightarrow \infty]/\lim[(Q)\ v \rightarrow 0]$ (where v is the potential scanning rate, V s^{-1}), represents a sound index of electrochemical porosity/activity of the material.

In fact, as it has been observed in many instances [55, 56], Q's may not be constant with v, and typically they result to linearly depend on $v^{-1/2}$, thus clearly suggesting the presence of diffusion limited phenomena. The direct extrapolation to $v^{-1/2} \rightarrow 0$, that is $v \rightarrow \infty$, defines the "outer" voltammetric area, Q_{out}, i.e. the quantity of charge that can be most easily and rapidly accumulated by the oxide layer. Parallelly, $1/Q$ varies linearly with $v^{1/2}$, hence the extrapolation to $v \rightarrow 0$ allows the definition of a "total" voltammetric area, Q_{tot}, which represents the maximum storable charge. Finally, the difference $Q_{in} = Q_{tot} - Q_{out}$ defines the "inner" area, the quantity of charge that is accumulated or exchanged on a longer timescale.

As evidenced by Fierro et al. [57], two explanations have been given for the dependence of the voltammetric charge on the scan rate. The first one, originally proposed by Ardizzone et al. [55] relates the dependence of Q to the proton diffusion inside the porous oxide matrix. At high scan rates only the most "accessible" sites are involved in the charging process, while at low scan rates also the "poorly accessible" sites are reached by the diffusing protons.

More recently [58], other two phenomena were considered in detail in the case of glassy carbon-supported RuO_2, namely the double layer charging, and its related capacitance which is independent on v, and the adsorption/desorption of the electrolyte ions, which determines a variation of capacitance inversely proportional to the potential scan rate.

To our opinion, the two points of view can be unified: the double layer capacitance (whose share has been quantified by [57]) is bound to the particle surface charging and is independent on scan rate; thus its contribution is embedded into Q_{out}, i.e. it represents a fraction of the most accessible sites. Pseudo-capacitive, i.e. faradaic surface phenomena, account for both fast and slow charge storage sites, in dependence on the proton diffusion hindrance, which in turn depends on the material morphology and phase composition.

While the ion adsorption contribution can be zeroed by the selection of the appropriate electrolyte (e.g. 0.1 M $HClO_4$), the splitting between the other two would require the introduction of a new experimental variable, e.g. temperature as proposed by [57].

Nonetheless, Q_{tot} preserves its role of cumulative electrochemical active surface parameter, as evidenced in Figs. 7–9. In particular, Fig. 7 refers to the comparison between the Ti-SnIr_550 electrode and the C-ME filled with the SnIr_550 powder (C-ME-SnIr_550), after normalization of the respective currents, as obtained by I/Q_{tot} (A C^{-1}). The two curves, which on the I scale would be separated by more than 5 orders of magnitude, results fully comparable on the I/Q scale, thus confirming the total

equivalence between the Ti-supported materials and the unsupported powders. In addition, the better behaviour of the Ti-SnIr_550 in terms of contact resistance is also evident. In fact, the slightly sloping shape of C-ME-SnIr_550 denotes a non negligible internal resistance, bound to a less densely packed powder.

Figures 8 and 9 collect the CV's (0.4–1.4 V, 20 mV s^{-1}) and the quasi steady-state polarization curves (1.4–2.0 V) for the three Ti–$Sn_{0.15}Ir_{0.85}O_2$ samples, calcined at 450, 500, and 550 °C respectively. All CV's show high symmetry between the cathodic and the anodic scans, together with the typical broad peaks of the IrO_2-rich mixed oxides [18]. Analogously, all the polarization curves exhibit parallel trends, with slopes, evaluated at low overpotentials and listed in the caption, showing that no significant differences are observed between the mechanisms of the OER on the three electrodes. In both cases the current values increase with the decreasing of the calcination temperature, in line with the decreasing of particle sintering. Upon normalization, that is upon dividing the current values by Q_{tot}, I/Q_{tot} (A C^{-1}), the three samples exhibit almost overlapping features (see Fig. 8b Fig. 9 b).

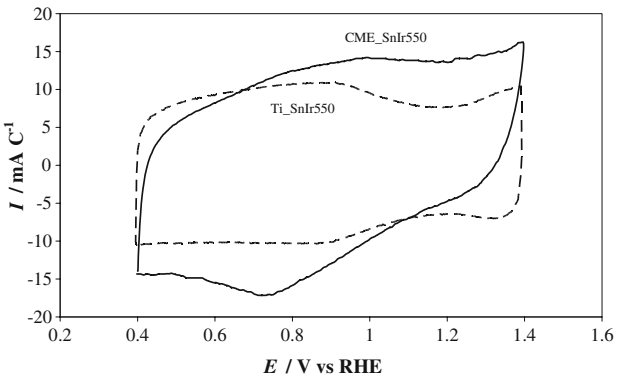

Fig. 7 Cyclic voltammograms recorded on (*dashed line*) Ti–SnIr_550 and (*full line*) C-ME-SnIr_550 electrodes. Currents are normalized by Q_{tot}. Curves were recorded at 20 mV s^{-1} in the 0.4–1.4 V potential range in 0.1 M $HClO_4$

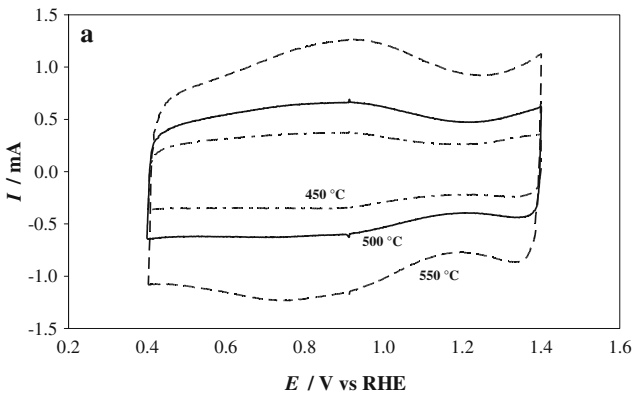

Fig. 8 Cyclic voltammograms recorded on Ti–$Sn_{0.85}Ir_{0.15}O_2$ electrodes calcined at three different calcination temperatures: (*dash-and-dot line*) 450 °C, (*full line*) 500 °C and (*dashed line*) 550 °C, (**a**) as recorded or (**b**) normalized by Q_{tot}. Curves were recorded at 20 mV s^{-1} in the 0.4–1.4 V potential range in 0.1 M $HClO_4$

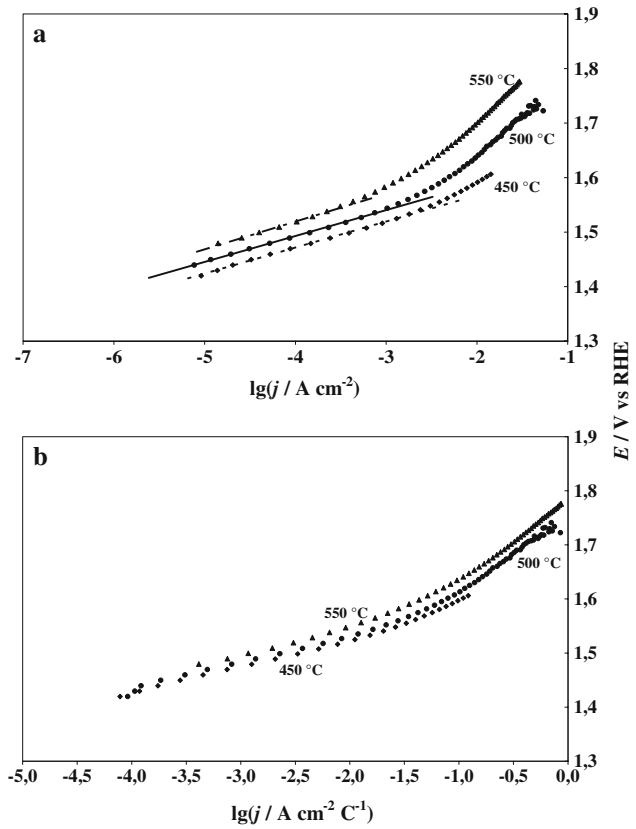

Fig. 9 (**a**) Quasi steady-state polarization curves (corrected by ohmic drops) recorded on Ti–$Sn_{0.85}Ir_{0.15}O_2$ electrodes calcined at three different calcination temperatures: (*lozenges*) 450 °C, (*circles*) 500 °C, (*triangles*) 550 °C. Lines show the linear regressions with slopes of (*dashed line*) 47.9 mV $decade^{-1}$, (*full line*) 47.5 mV $decade^{-1}$, and (*dash-and-dot line*) 52.4 mV $decade^{-1}$ for the samples calcined at 450, 500 and 550 °C respectively. (**b**) The same curves of Fig. 9a normalized by Q_{tot}. Curves were recorded stepwise at 10 mV min^{-1} in the 1.4–2.0 V potential range in 0.1 M $HClO_4$

Further information can be gathered by the inspection of the Q_{out}/Q_{tot} ratio, the so-called "electrochemical porosity" [30], for which a non monotonic dependence on the calcination temperature is observed: 0.80 at 450 °C, 0.78 at 500 °C and 0.82 at 550 °C. This behaviour reflects the articulated role that the firing temperature plays on the various properties of the powders (e.g. phase composition, Ir speciation, surface and bulk chemical composition and morphology), as described in the previous paragraphs.

4 Discussion

The present synthetic route, based on the combination of a sol–gel stage and of a subsequent calcination treatment, has led to the formation of nanostructured materials with variable features. The results of the different characterizations, presented in the previous sections, are quite convergent with one another and jointly show that even slight variations of the temperature adopted for the final firing are sufficient to provoke relevant modifications in all the features of the particles either structural, morphological, superficial or electrochemical.

X-ray and Raman show that Ir can substitute Sn in the lattice at any temperature. This is a relevant result since much debate is present in the literature with respect to the actual formation of a stable or metastable solid solution between SnO_2 and IrO_2. The present results show, however, that the volume of the unit cell is not a monotonic function of the temperature but it shows a minimum, i.e. the largest distortion, at 500 °C. Apparently this temperature gives rise to the best solubility conditions of Ir in the cassiterite lattice since, only at this temperature, all the Ir ions added in the synthesis appear to be incorporated in the host structure. Hence, the formation of a solid solution is the result of a subtle balance between diverging mechanisms which are markedly affected by the temperature. In fact a slight increase in the calcination temperatures (from 500 to 550 °C) leads to the formation of a different system: a solid solution with less Ir in the lattice with respect to 500 °C and in the presence of a minor amount of a separate IrO_2 phase. The firing at 450 °C, instead, seems to leave a fraction of the Ir starting salt still not fully reacted.

Direct characterizations of the product morphology (TEM, HRTEM) indicate that the crystallites are spherical with a relatively narrow size distribution. The size of the crystallites and particles are also tuned by the temperature of the firing and by the presence of Ir. The size almost halves by addition of Ir with respect to pure SnO_2 and simultaneously decreases with the lowering of the firing temperature. The various adopted characterizations show different sides of this effect; the decrease in the crystallite sizes is paralleled by the increase in the specific surface area, which, in its turn, is mirrored by the marked increase in the Raman mode attributed to the surface.

By XPS further aspects related to the speciation of Ir can be appreciated. The peak of Ir 4f is in any case the result of the presence of several components representative of different oxidation states of the metal in the oxide (III, IV, > IV). By increasing the firing temperature the progressive modification in the shape of the peak indicates a progressive enrichment in the more oxidized species.

The way the physico-chemical features, observed by the different characterizations, affect the charging and transport properties of the composites is very interesting to comment. A priori, in fact, the electrochemical response, at least in terms of accessibility of active sites, that is the Q_{out}/Q_{tot} ratio, could have been expected to show a simple decreasing trend with temperature of firing, just following the decrease of the specific surface area and/or the relative crystallite growth. Actually it is not so and the fraction of accessible active sites show a common non monotonic trend with temperature, the quantity determined for the sample calcined at 500 °C (SnIr_500) representing the lower end of the series. This behaviour, which points to a lower-defectivity material, is in agreement with XRD and Raman data, according to which there is a total reticular substitution of Sn by the added Ir. The lowest Q_{out}/Q_{tot} ratio would then be bound to hindrance of the Ir centres which govern the surface charging processes. Parallelly, the SnIr_550 powder, for which a partial segregation of IrO_2 is suggested, exhibits the highest values for the voltammetric ratio to denote larger electrochemical activity and porosity. Very likely the intermediate behaviour of SnIr_450 comes from the balance between diverging aspects, like the higher thickness of the Raman-detected defective layer, the incomplete hydrolysis/combustion of the starting Ir salt, the higher Ir(III) surface content, responsible for an high pseudo-capacitance contribution to the charge accumulation, and the highest BET area.

Obviously, these considerations cannot include any forecast on the actual performances of the final materials, since any application calls for the achievement of a particular combination of phase and chemical composition/morphology.

In the particular case of electrocatalysis, we think that the selected firing temperature range is the most interesting since it represent, as highlighted by experimental evidences, the best compromise between surface area extension, expected stability and phase composition.

Firing temperature lower than 450 would lead to a very high surface area but low expected stability material thus decreasing its overall applicability. At the same time, temperatures higher than 550 °C would lead to high sintherization (i.e. lower surface area extension) and to a

very low defectivity, likely decreasing the performances, despite a possible increase of IrO_2 surface segregation, both in terms of charge storage and activity toward oxygen production/reduction.

In summary, the electrochemical response appears not to be a simple function of one of the properties but to be the outcome of an interplay between intertwined and, in some cases, counterposing factors: the partition of Ir species between the reticular cassiterite positions and separate phases, the particle morphology and the Ir speciation in the composite.

5 Conclusions

Sn–Ir composites at low Ir content (15 mol%) are obtained by following a sol–gel procedure combined with thermal treatments performed in the range 450–550 °C.

The features of the composites are finely modulated by both the temperature of firing and by the presence of Ir in the cassiterite lattice. The lower the temperature the higher the surface area and the smaller the crystallite size. The addition of Ir further inhibits the crystal growth and makes the external layers of the particles more disordered.

The trend of the surface area with the calcination temperature apparently governs the electrochemical behaviour in both potential windows, that is in the pseudo-capacitive, and in the OER regions. This macroscopic effect can be mostly compensated by the normalizing action of Q_{tot}, i.e. the total number of active sites, to let more subtle features to become evident. In agreement with the ex-situ characterizations, these properties are not monotone with the calcination temperature. In particular, 450 °C calcined materials are attractive because of their higher defectivity, which is an important feature for fast charge-exchange processes. At the other extreme, the 550 °C samples provide a promising surface enrichment of the active Ir centres. In the middle, the 500 °C composites seem to offer the highest stability thanks to their ordered structure.

Acknowledgements Financial support from the Ministry of Education, University and Research and Università degli Studi di Milano (FIRST Funds) is gratefully acknowledged.

References

1. Izutsu K, Yamamoto H (1996) Anal Sci 12:905
2. Yao S, Wang M, Madou M (2001) J Electrochem Soc 148:H29
3. Patil PS, Kawar RK, Sadale SB (2005) Appl Surf Sci 249:367
4. Gottesfeld S, MnIntyre JDE, Beni G, Shay JL (1978) Appl Phys Lett 33:208
5. Savinell RF, Zeller RLIII, Adams JA (1990) J Eletcrochem Soc 137:489
6. Ribeiro J, Alves PDP, De Andrade AR (2007) J Mat Sci 42:9293
7. Marshall A, Borresen B, Hagen G, Tsypkin M, Tunold R (2005) Mater Chem Phys 94:226
8. Marshall A, Tsypkin M, Borresen B, Hagen G, Tunold R (2004) J New Mater Electrochem Syst 7:197
9. Cardarelli F, Taxil P, Savall A, Comninellis Ch, Manoli G, Leclerc O (1998) J Appl Electrochem 28:245
10. Horvath E, Kristof J, Frost RL, Heider N, Vagvolgyi V (2004) J Thermal Anal Calorim 78:687
11. Alves VA, da Silva LA, Oliveira ED, Boots JFC (1998) Mater Sci Forum 282:655
12. Chen X, Chen G (2005) J Electrochem Soc 152:J59
13. Chen X, Chen G, Yue PL (2001) J Phys Chem B 105:4623
14. Ardizzone S, Bianchi CL, Cappelletti G, Ionita M, Minguzzi A, Rondinini S, Vertova A (2006) J Electroanal Chem 589:160
15. Comninellis Ch, Vercesi GP (1991) J Appl Electrochem 21:335
16. Ortiz PI, De Pauli CP, Trasatti S (2004) J New Mater Electrochem Syst 7:153
17. De Pauli CP, Trasatti S (2002) J Electroanal Chem 538:145
18. De Pauli CP, Trasatti S (1995) J Electroanal Chem 396:161
19. Marshall A, Borresen B, Hagen G, Sunde S, Tsypkin M, Tunold R (2006) Russ J Electrochem 42:1134
20. Rasten E (2001) Electroctalysis in water electrolysis with solid polymer electrolyte. PhD Thesis, NTNU, Trondheim, Norway
21. Grupioni AAF, Arashiro E, Lassali TAF (2002) Electrochim Acta 48:407
22. Yoshinaga N, Sugimoto W, Takasu Y (2008) Electrochim Acta 54:566
23. Takasu Y, Yoshinaga N, Sugimoto W (2008) Electrochem Comm 10:668
24. D'Urso C, Morales LS, Di Blasi A, Baglio E, Ornelas R, Orozco G, Arriaga LG, Antonucci V, Aricò A (2007) ECS Trans 11:191
25. Trasatti S (2001) Port Electrochim Acta 19:197
26. Burke LD, Naser NS, Ahern BM (2007) J Solid State Electrochem 11:655
27. Shibli SMA, Dilimon VS (2007) J Solid State Electrochem 11:1119
28. Tian M, Bakovic L, Chen A (2007) Electrochim Acta 52:6517
29. Vázquez-Gómez L, Horváth E, Kristóf J, Rédey Á, De Battisti A (2006) Appl Surf Sci 253:1178
30. Ardizzone S, Cappelletti G, Ionita M, Minguzzi A, Rondinini S, Vertova A (2005) Electrochim Acta 50:4419
31. Ionita M, Cappelletti G, Minguzzi A, Ardizzone S, Bianchi CL, Rondinini S, Vertova A (2006) J Nanopart Res 8:653
32. Cachet-Vivier C, Vivier V, Cha CS, Nedelec J-Y, Yu LT (2001) Electrochim Acta 47:181
33. Vertova A, Barhdadi R, Cachet-Vivier C, Locatelli C, Minguzzi A, Nedelec J-Y, Rondinini S (2008) J Appl Electrochem 38:965
34. Larson AC, Von Dreele RB (1994) GSAS: General Structural Analysis System. Los Alamos National Laboratory, Los Alamos, NM
35. Toby BH (2001) J Appl Crystallogr 34:210
36. Cappelletti G, Ricci C, Ardizzone S, Parola C, Anedda A (2005) J Phys Chem B 109:4448
37. Shirley D (1972) Phys Rev B 5:4709
38. Chantrell RW, Popplewell J, Charles SW (1977) Physica 86-88B:1421
39. Vivier V, Cachet-Vivier C, Wu BL, Cha CS, Nedelec J-Y, Yu LT (1999) Electrochem Solid-State Lett 2:385
40. Cachet-Vivier C, Vivier V, Cha CS, Nedelec J-Y, Yu LT (2001) J Electrochem Soc 148:E177
41. Hume-Rothery W, Raynor G (1954) The structure of metals and alloys. Institute of Metals, London
42. Murakami Y, Ohkawauchi H, Ito M, Yahiikozawa K, Takasu Y (1994) Electrochim Acta 39:2551
43. Liu Y, Li Z, Li J (2004) Acta Mater 52:721
44. Reames F (1976) Mater Res Bull 11:1091

45. Chuu DS, Dai CM, Hsieh WF, Tsai CT (1991) J Appl Phys 69:8402
46. Zuo J, Xu C, Liu X, Wang C, Wang C, Hu Y, Qian Y (1994) J Appl Phys 75:1835
47. Dieguez A, Romano-Rodriguez A, Vilà A, Morante JR (2001) J Appl Phys 90:1550
48. Moulder JF, Stickle WF, Bomben KD (1992) Handbook of X-ray photoelectron spectroscopy. Perkin Elmer, Eden Priaerie
49. Atanasoska L, Atanasoski R, Trasatti S (1990) Vacuum 40:91
50. Da Silva LM, Franco DV, De Faria LA, Boodts JFC (2004) Electrochim Acta 49:3977
51. Hara M, Assami K, Hashimoto K, Matsumoto T (1983) Electrochim Acta 28:1073
52. Chen RS, Chang HM, Huang YS, Tsai DS, Chattopadhyay S, Chen KH (2004) J Cryst Growth 271:105
53. Koetz R, Neff H, Stucki S (1984) J Electrochem Soc 131:72
54. Ardizzone S, Carugati A, Trasatti S (1981) J Electroanal Chem 126:287
55. Ardizzone S, Fregonara G, Trasatti S (1990) Electrochim Acta 35:263
56. Krstajic N, Trasatti S (1998) J Appl Electrochem 28:1291
57. Fierro S, Ouattara L, Herrera Calderon E, Comninellis Ch (2008) Electrochem Comm 10:955
58. Sugimoto W, Kizaki T, Yokoshima K, Murakami Y, Takasu Y (2004) Electrochim Acta 49:313